Influence of laser powder bed fusion scanning pattern on residual stress and microstructure of alloy 718

J. Čapek [a,*], E. Polatidis [a], N. Casati [b], R. Pederson [c], C. Lyphout [d], M. Strobl [a]

[a] Laboratory for Neutron Scattering and Imaging, Paul Scherrer Institute, CH-5232 Villigen PSI, Switzerland
[b] Materials Science Group, Photon Science Division, Paul Scherrer Institute, 5232 Villigen-PSI, Switzerland
[c] University West, 46132 Trollhättan, Sweden
[d] Department of Manufacturing, RISE IVF AB, Mölndal, Sweden

HIGHLIGHTS

- Detail microstructural analysis using electron microscopy and synchrotron X-Ray diffraction was done.
- Four phases were identified and their volume fraction was quantified.
- Residual stresses were evaluated and the problematics of stress free sample was discussed in detail.
- It was observed that the selection of the scanning path can have same effect as a change of the processing parameters.

GRAPHICAL ABSTRACT
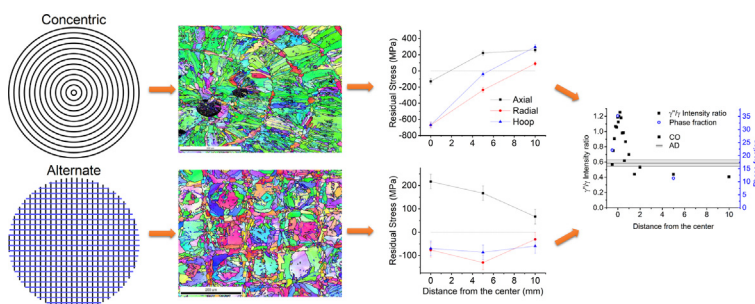
ABSTRACT

A comprehensive investigation is undertaken on the effect of laser scanning pattern on the microstructure of cylindrical samples made of Alloy 718 processed by Laser Powder Bed Fusion. It is observed that the common alternate direction scanning of the laser results in a more homogeneous microstructure than the less common concentric line scans where significant microstructural heterogeneities are seen between the edges and the center of the sample. The investigation focuses on the precipitation, crystallographic texture, grain size, grain morphology and residual stresses utilizing synchrotron X-ray diffraction, neutron diffraction and electron microscopy. The heterogeneous microstructure of the sample processed with the concentric laser pattern influences the chemical composition of the matrix, which alters the reference "strain free" interplanar spacing used for evaluating the residual strain. The investigation underlines the significance of the processing parameters on the homogeneity of the microstructure and the effect of the chemical variations on the determination of residual stresses in materials such as Alloy 718, where strong local chemical variations occur because of different types and extent of precipitation.

© 2022 Published by Elsevier Ltd. This is an open access article under the CC BY-NC-ND license (http://creativecommons.org/licenses/by-nc-nd/4.0/).

1. Introduction

With the appearance of modern additive manufacturing (AM) processes, such as Laser Powder Bed Fusion (LPBF), building complex components of metallic materials has become highly attractive for many corresponding applications. The layer-by-layer manufacturing process allows building complex structures, which

* Corresponding author at: Forschungsstrasse 111, WBBA/113, 5232 Villigen PSI, Switzerland.
  E-mail address: jan.capek@psi.ch (J. Čapek).

are not feasible by conventional manufacturing methods. Various building parameters influence the microstructure and a significant ongoing effort focuses on this aspect, e.g. controlling the crystallographic texture, grain size or precipitation and phases [1–4]. In contrast, still significant challenges remain, such as building defects like porosity, cracking, lack of fusion, residual stresses (RS) and undesired microstructure heterogeneities need to be overcome or controlled [1]. There are multiple LPBF process parameters that can be varied and influence the defects, microstructure or RS. It has been shown that the energy density has a direct impact on porosity [5,6], the variation of scan speed and laser power greatly affects the crystallographic texture [6,7], and also the grain size and morphology are influenced by the processing parameters [8]. The RS are a result of the thermal expansion mismatches during the thermal cycles that the material undergoes [9] and hence, several studies focus on the influence of the processing parameters on RS both experimentally [10–15] and with modeling [16,17].

Components from nickel-based superalloys such as Alloy 718 processed by AM methods are highly attractive for several applications in the aerospace/automotive industry, chemical industry or nuclear industry as they exhibit good corrosion resistance, and good mechanical/creep properties at elevated temperatures [1]. However, the mechanical properties of these materials are especially sensitive to building conditions and post-treatment, as they are susceptible to forming secondary phase precipitates that alter their mechanical properties [18]. In general, the studies so far postulate the heterogeneity of the microstructure of the as-LPBF processed Alloy 718 containing a mixture of the matrix γ-phase with precipitates of γ"-phase [15] together with Laves [19,20] and MC-type carbides [19–21]. As such, the microstructural heterogeneity in the as-processed LPBF parts leads to mechanical heterogeneity. Hence, post-processing like Hot Isostatic Pressing (HIP)[22], heat treatments or a combination of both [23] are necessary to achieve densification and a homogeneous microstructure with well-controlled precipitation [24] which simultaneously lead to relief of the RS [21]. There has been significant work on the effect of process parameters on the RS. It is generally observed that the RS are higher in the direction of the scan vector than in the transverse direction [25,26] and recent studies suggest that rotation between each layer and using 45° line scans for rectangular samples helps reduce the RS [25,27]. Despite the optimization of the processes, the presence of RS is unavoidable and the current challenge is to suppress the RS as much as possible already during the LPBF process, to avoid wrapping, distortion, delamination and cracking, while the remnant RS, after the removal of the base plate, can be relieved with post-built heat treatments [19,28]. As the microstructure in many alloys is very sensitive to the annealing conditions, the temperature and time of annealing need to be carefully chosen and the initial (i.e. as-LPBF built) microstructure needs to be known, so that the evolving microstructure during annealing is well-controlled.

To produce tailored components with desired microstructures and mechanical properties fundamental knowledge about the mechanism of microstructure development and evolution during the LPBF process of metallic alloys is required. Moreover, being able to control the RS and the microstructure already during the AM processes is invaluable and bares the promise of being able to reduce the required number of production steps, and hence the lead time and investment cost. Within this effort, computational simulations have become a promising alternative to the cost and time-consuming parametric experimental investigations of LPBF components towards understanding the influence of the process parameters on the material properties. The models used for simulating the LPBF processes can predict the microstructure and RS based on the processing parameters. A fundamental property that manifests the material properties is the melt pool characteristics and hence, finite element or phase field models are used to predict the melt pool parameters [29,30]. Determining the shape of the melt pool helped understanding porosity [30], crystallographic texture [7] and grain morphology [17,31]. By simulating the entire AM process of an entire component and the associated thermal gradients and cycles, it is also possible to predict the development of RS in specific components [16,32]. Finally, analytical tools have been able to help predict the variation and evolution of different phases in metastable alloys [33]. A necessary precondition for the development of such kind of simulation tools is to collect enough experimental data, associating the process parameters with the resulting microstructure and the RS distribution that can be used for developing and validating the constitutive equations and models. Finally, due to the variability of the material properties between different samples, even when a single process parameter is altered, it is essential that the RS and microstructure characterization information is obtained from the very same sample, which has not been done in any of the above-mentioned studies.

In this study, we perform a comprehensive characterization of different as LPBF-built samples from Alloy 718 built with the same building parameters except for the laser scanning path. The investigation highlights the strong effect of the laser scanning path on the sample microstructure, on the RS variation within the sample and the challenge of obtaining a reliable "strain-free" standard for the assessment of RS. Neutron diffraction is utilized for the characterization of RS, Electron Back Scattered Diffraction (EBSD) for characterizing the crystallographic texture, grain morphology and precipitation and synchrotron X-ray diffraction for the identification of the microstructural heterogeneity and for revealing the phases present in the microstructure. Finally, this investigation is the first part of a comprehensive investigation on the optimization of annealing temperatures/times for relieving the RS while controlling the microstructure of the end product.

2. Experimental methods

Two types of cylindrical samples with 25 mm in diameter and 10 mm height were produced with the same process parameters, but different scanning patterns i.e. one alternate scanning where, for every layer, the laser travels along lines with alternate direction (hereafter denoted with AD sample) and one concentric (hereafter denoted with CO sample) where, for every layer, the laser travels in circles going from the outer surface to the center of the cylinder. A schematic of the scanning strategies is show in Fig. 1. The processing parameters were: laser power: 200 W, scanning speed: 900 mm/s, hatching spacing: 120 μm and layer thickness: 30 μm. The base plate was preheated to 100 °C.

The microstructure of the samples was characterized by EBSD. The samples were ground with 4000 grit SiC paper, polished down to 0.25 μm with diamond paste and then electro-polished with a solution of 70 ml H_2O, 200 ml glycerol, 720 ml H_2SO_4 at 40 V for 30 s. A field emission gun scanning electron microscope (FEG SEM) Zeiss ULTRA 55 equipped with EDAX Hikari Camera operated at 20 kV in high current mode with 120 μm aperture size. The EBSD raw data was post-processed using the EDAX OIM Analysis 7.3 software.

Diffraction methods were used to evaluate the RS in the sample. RS can be calculated according to Eq. (1) by measuring the lattice strains along the three principal directions of the sample. Due to the building strategies and the four-fold (for the AD) or cylindrical (for the CO) symmetry of the samples, these axes correspond to the building direction, the two perpendicular laser scan directions for the alternate scanning and two random perpendicular directions
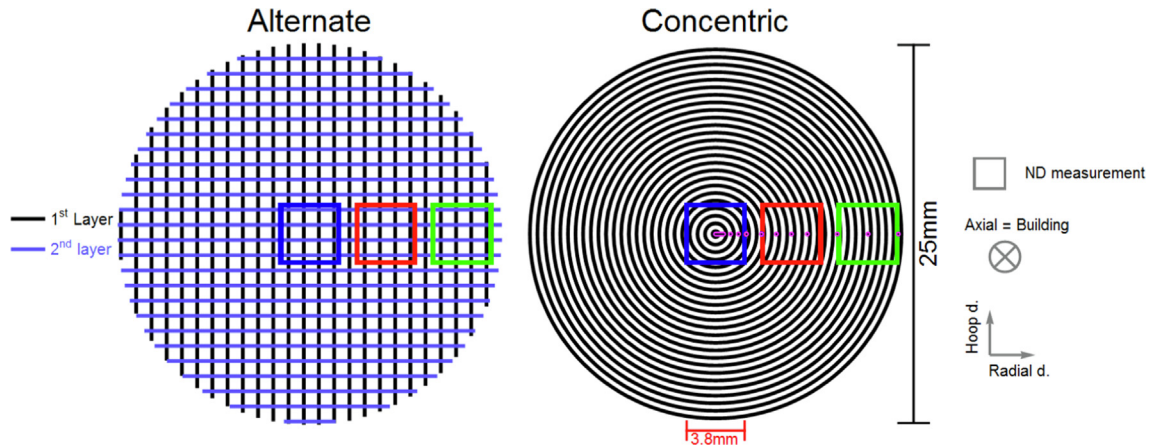
Fig. 1. Schematic of scanning patterns and the areas of ND and XRD.

for the concentric scanning sample, respectively (see Fig. 1). The lattice strain is calculated using Eq. (2) comparing the stressed lattice spacing, d_{hkl}, of the *hkl* family of lattice planes, to the lattice spacing of a reference, "stress free" sample, $d_{0,hkl}$.

$$
\begin{pmatrix} \sigma_{11} \\ \sigma_{22} \\ \sigma_{33} \end{pmatrix} = \frac{E_{hkl}}{(1+v_{hkl})(1-2v_{hkl})} \begin{pmatrix} 1-v_{hkl} & v_{hkl} & v_{hkl} \\ v_{hkl} & 1-v_{hkl} & v_{hkl} \\ v_{hkl} & v_{hkl} & 1-v_{hkl} \end{pmatrix}
$$
$$
\times \begin{pmatrix} \varepsilon_{11,hkl} \\ \varepsilon_{22,hkl} \\ \varepsilon_{33,hkl} \end{pmatrix} \tag{1}
$$

$$
\varepsilon_{hkl} = \frac{d_{hkl} - d_{0,hkl}}{d_{0,hkl}} \tag{2}
$$

Neutron diffraction (ND) experiments were carried out at the time-of-flight diffractometer POLDI at the Swiss Spallation Source, SINQ at the Paul Scherrer Institute, Switzerland. Three positions were selected for the ND measurements (center, 5 mm and 10 mm radial distance from the center) (Fig. 1). A gauge volume of 3.8 × 3.8 × 3.8 mm³ was defined by a pair of diaphragms in the incident beam and a radial collimator in the diffracted beam. The obtained data were fitted using a Gaussian function in Mantid [34] to obtain the peak positions, full-width at half maximum and integrated intensity of the diffraction peaks, which were further analyzed using in-house Wolfram Mathematica scripts. The error bars are taken from the standard error of the fitted peak position. Standard method for the propagation of uncertainty was used. For the residual strain estimation, the 3 1 1 diffraction peak was used as it is the least affected by the intragranular strain and interphase strains [35]. For calculating the corresponding stress the plane specific elastic properties of E_{311} = 200 GPa and v_{311} = 0.33 [36] were used in eq. (1).

Alloy 718 has face-centered cubic matrix γ and its superior mechanical behavior is due to the presence of coherent and semi-coherent γ' and γ'' phase [37] (see Fig. 2. In contrast to the beneficial γ' and γ'' phases, the presence of δ phase and the Laves phase result in loss of ductility and higher tendency for high temperature cracking [38–41]. In addition to the above-mentioned precipitates, niobium and titanium carbides often also form in Alloy 718. Large variations of the lattice parameters can be found in literature due the difference in nominal compositions, extend and type of precipitation that result in (local) variations in chemical composition and strain fields around the precipitates. In addition, the diffraction peaks of γ' and γ'' precipitates strongly overlap with the diffraction peaks of the matrix γ. Hence, using

synchrotron X-ray diffraction (XRD) for studying the precipitation fractions is essential as it offers the flux and resolution to identify and quantify the different phases (see Table 1).

In order to measure the "strain-free" lattice parameter and the phase composition, a thin stripe (100 μm in thickness) was cut from the samples with electrical discharge machining (EDM) and XRD measurements were undertaken at the MS beamline at the Swiss Light Source, SLS, at the Paul Scherrer Institute, Switzerland using 25 keV energy and a 100 × 100 μm² spot size. The measurements were undertaken in transmission using a Pilatus 6 M detector to capture the entire Debye Scherrer rings. The diffraction data were calibrated using a LaB6 standard and integrated along the entire azimuthal range using the open source software bubble [42]. The diffraction patterns were fitted with single-peak fitting using in-house Mathematica codes for obtaining the peak positions, FWHM and peak intensity. Rietveld refinement was performed using the open access software GSAS-2 [43] for obtaining the phase fraction. 17 points were measured for the CO sample at −0.5, −0.4, −0.3, −0.2, −0.1, 0, 0.05, 0.1, 0.2, 0.3, 0.4, 0.5, 0.7, 1, 1.5, 2, 5, 10 mm radial distance from the center, since strong variations of the d values were expected. Several radially distributed points were measured for the AD sample as well as points close to the building plate and top of the sample to investigate the influence of the distance from the base plate.

3. Results

3.1. Neutron diffraction - lattice parameters

The ND data were analyzed in terms of intensity and peak position in order to evaluate the texture and microstrains. The four strongest diffraction peaks are plotted in Fig. 3. The 2 2 0 peak is the strongest in the building direction for both samples indicating a strong ⟨1 1 0⟩ -texture. The texture is homogenous throughout the entire AD sample along the hoop and radial directions and there is no significant difference between hoop and radial direction. For the CO sample the strongest ⟨1 1 0⟩ -texture appears in the center and it becomes less sharp towards the edge of the sample, as apparent by the decrease in the intensity of the 2 2 0 peak. The intensity of the 2 0 0 peak increases progressively from the center to the edge in the hoop direction. In this case, the hoop direction is aligned with the laser scanning direction.

The lattice spacing for two lattice plane families ({2 0 0},{3 1 1}) are shown in Fig. 4. The AD sample exhibits less d-spacing variation than the CO sample. For the AD sample, the lattice spacing in the radial and hoop directions have the same value within the
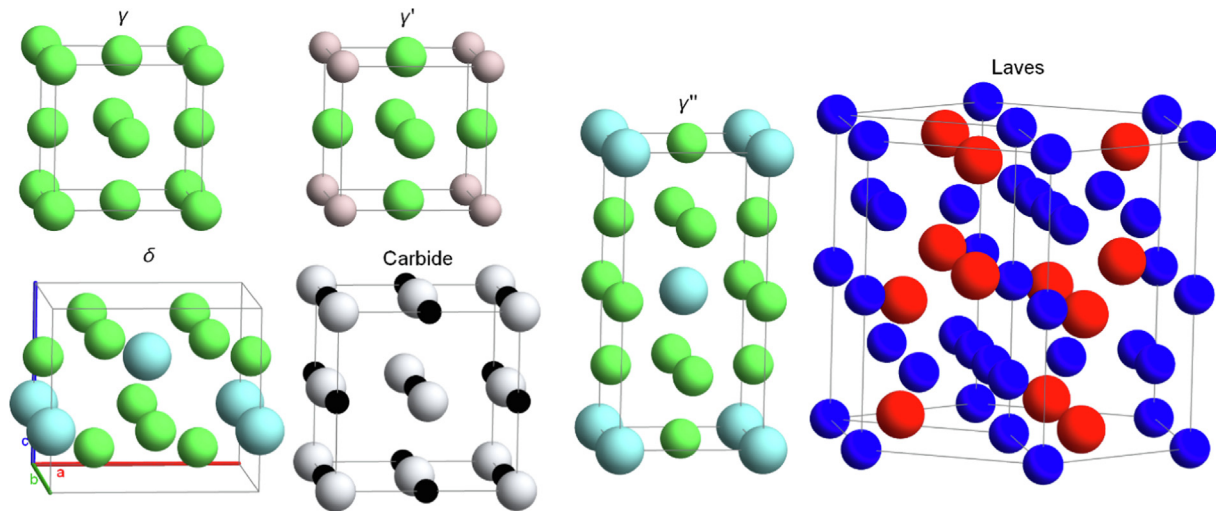
Fig. 2. Crystal structures for the possible phases in Alloy 718.

Table 1
Phases in the Alloy 718.

Phase	Composition	space group		Lattice parameters
γ	◼ Ni	225	F m-3 m	$a = 3.591 \pm 0.005$
γ'	◼ Ni ◼ Al	221	P m-3 m	$a = 3.564 \pm 0.004$
γ''	◼ Ni$_3$ ◼ Nb	139	I 4/m m m	$a = 3.624 \pm 0.005$, $c = 7.406 \pm 0.004$
δ	◼ Ni$_3$ ◼ Nb	59	P m m n	$a = 5.11 \pm 0.01$, $b = 4.23 \pm 0.02$, $c = 4.54 \pm 0.02$
Carbide	◼ C ◼ Ti/Nb	225	F m-3 m	$a = 4.506(NbC)$, $a = 4.327(TiC)$
Laves	◼ (NiFeCr)$_2$ ◼ (TiMoNb)	194	P 63/m m c	$a = 4.774$, $c = 7.759$

experimental error, which is lower than for the axial direction. The CO sample exhibits much higher differences between the lattice spacing along the three measured scattering vectors. Similarly, to the AD sample, the lattice spacing in the radial and hoop directions have the same value in the center, which is lower than the axial one for the CO sample. The lattice spacing in the hoop direction significantly increases towards the edge of the sample, reaching the value of the lattice spacing in the axial direction while the lattice spacing in the radial direction increases only slightly.

3.2. Xrd

The XRD patterns were analyzed for the phase composition of the samples (Fig. 5). Four phases were identified in the as built samples: the γ matrix and γ'' phase, Laves phase and carbides in form of precipitates. No reflections corresponding to delta or γ' were identified.

Rietveld analysis (Fig. 5a) was performed on 3 diffraction patterns, in the center, at −0.5 mm and at 5 mm from the center for the CO sample. The wR values for the fits are less than 10% (i.e. 7.05% and 4.45%). Both fits suggest that the phase fraction of the carbides is less than 1% and the fraction of Laves around 3%, while the variation through the sample is within the experimental error. Compared to that it is possible to observe strong variation in the γ'' precipitate fraction, as shown in Table 2.

Rietveld analysis becomes very challenging when combining all 4 existing phases, where especially γ and γ'' peaks strongly overlap. Therefore, instead of Rietveld refinement, single peak fitting was used to analyze the phase fractions semi-quantitatively. As shown in Fig. 5(b) the γ and γ'' peaks overlap strongly which results in relatively high uncertainty in defining their position and intensity.

The lower symmetry of the γ'' phase and the lattice parameters $2a \approx c \cap 2a \neq c$ results in splitting into 2 or 3 reflections of γ'' reflections. Fitting of such complex and overlapping groups of diffraction peaks becomes impossible. In order to follow the shift of the γ lattice parameter both diffraction peaks originating from γ and γ'' were fitted as a single peak. This approximation can cause some systematic error in the absolute values of peak positions and intensities; however, it does not influence the observed trends.

The single peak fitting results for the Laves phase and carbides are shown in Fig. 6 for the CO sample. The carbide phase clearly exhibits increase of the lattice parameter and small decrease of the FWHM towards the center of the sample. The values at the edge of the CO sample are similar to the values for the AD sample. The evolution of the lattice parameter for the Laves phase is not as clear as that of the carbide phases. It is seen that the a parameter (Fig. 6c) increases towards the center, similarly to the carbide phase. The c parameter (Fig. 6e) appears to increase at the proximity of the center, however it decreases at the center. Also, the FWHM difference is not as strong as the one for the carbides.

The evolution of the lattice parameters for the γ matrix is shown in Fig. 7. In contrast to the evolution of the lattice spacing in the carbides, the lattice parameter of the γ and γ'' phases decreases towards the center.

Another way to quantify the extent of γ'' precipitation is to use the $\frac{\sum I_{\gamma''}}{\sum I_\gamma}$ intensity ratio, where the sum of the integrated intensity of all measured γ peaks (i.e. 111, 200, 220, 311, 222, 400, 331, 420) and the corresponding γ'' peaks, within the accessible Q-range, are considered. Fig. 8a shows a close-up of a diffraction pattern at the position of the 311 peak, where the intensity is normalized by the peak height. It is possible to observe the increasing intensity of the
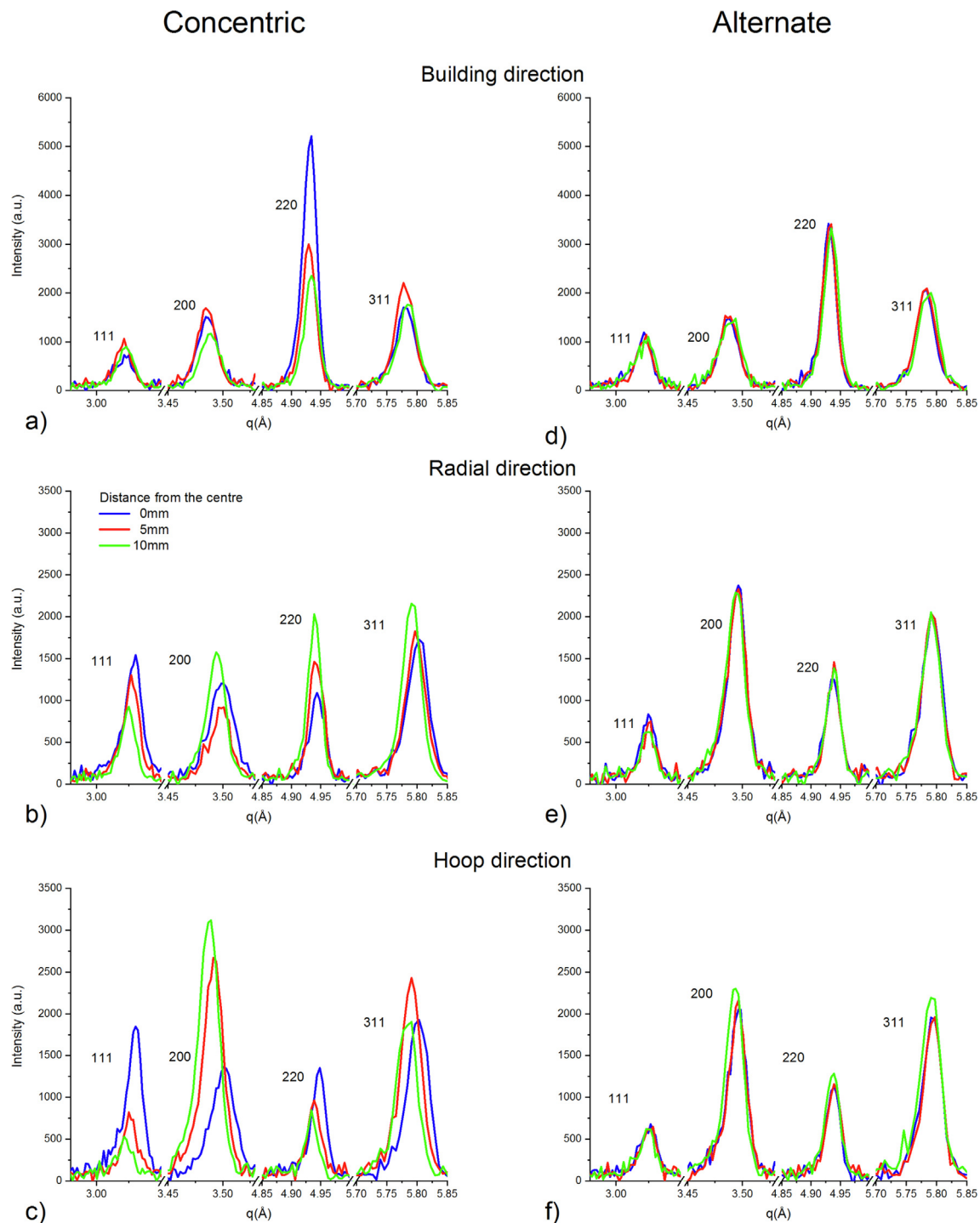
Fig. 3. Diffraction peaks for (a,d) building, (b,e) radial and (c,f) hoop direction, for both concentric (CO) and alternate scanning direction (AD) samples.

shoulder on the left side of the main peak towards the center of the sample, suggesting that the fraction of γ'' phase increases with annealing. The results from the γ''/γ ratio are compared to the results from the Rietveld refinement (Fig. 8b). The intensity ratio agrees well with the trend observed for the γ'' phase fraction obtained from the Rietveld refinement. The phase fraction of the γ'' is highest in the center in both cases and decreases towards the edge, as expected by the accumulation of heat at the center of the sample during the laser scanning.

Similar analysis was undertaken also for the AD sample. There is no significant variation observed radially, i.e. the γ'' phase fraction does not vary significantly between the outer surface and the center of the cylinder. However, the calculation of the γ''/γ intensity ratio shows statistically significant difference between the bottom $(\gamma''/\gamma)_{bottom} = 0.69 \pm 0.06$ and top $(\gamma''/\gamma)_{top} = 0.58 \pm 0.04$ part of the sample, suggesting that there is a higher γ'' phase fraction in the proximity of the base plate than close to the top
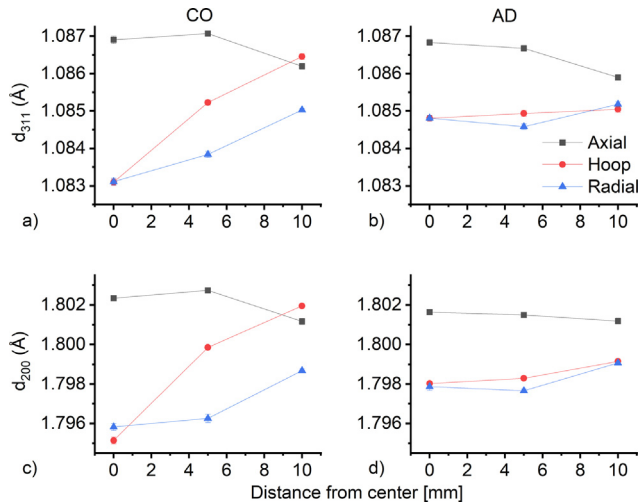
Fig. 4. Lattice spacing of the lattice plane families (a,b) {311}, (c,d) {200} for samples built with (a,c) concentric (CO) and (b,d) alternate scanning direction (AD) samples.

part. Such observation can be explained by the intrinsic heat treatment that the bottom layers experience as new layers are added.

3.3. Microstructure

The grain morphology of the AD sample correlates with the laser path. It is possible to observe the square grid pattern with large grains in the middle and smaller grains along the grid in the building plane, as shown in Fig. 9a. The square grid size is 120 μm, which correlates with the hatch spacing. The microstructure in the radial direction exhibits a columnar structure, which is typical for LPBF [44] Fig. 9b.

The crystallographic texture was evaluated from the EBSD by stitching several EBSD maps and these results were compared to the results from ND. The inverse pole figures (IPF) show mild ⟨110⟩ texture in the building direction of the AD sample (Fig. 9). The strength of the texture depends on the distance from the center. Both radial and hoop direction exhibit mild ⟨100⟩ texture.

Similar to the AD sample, the morphology of the microstructure of the CO sample is influenced by the laser travel path and resembles the concentric scanning pattern, as apparent by the EBSD map
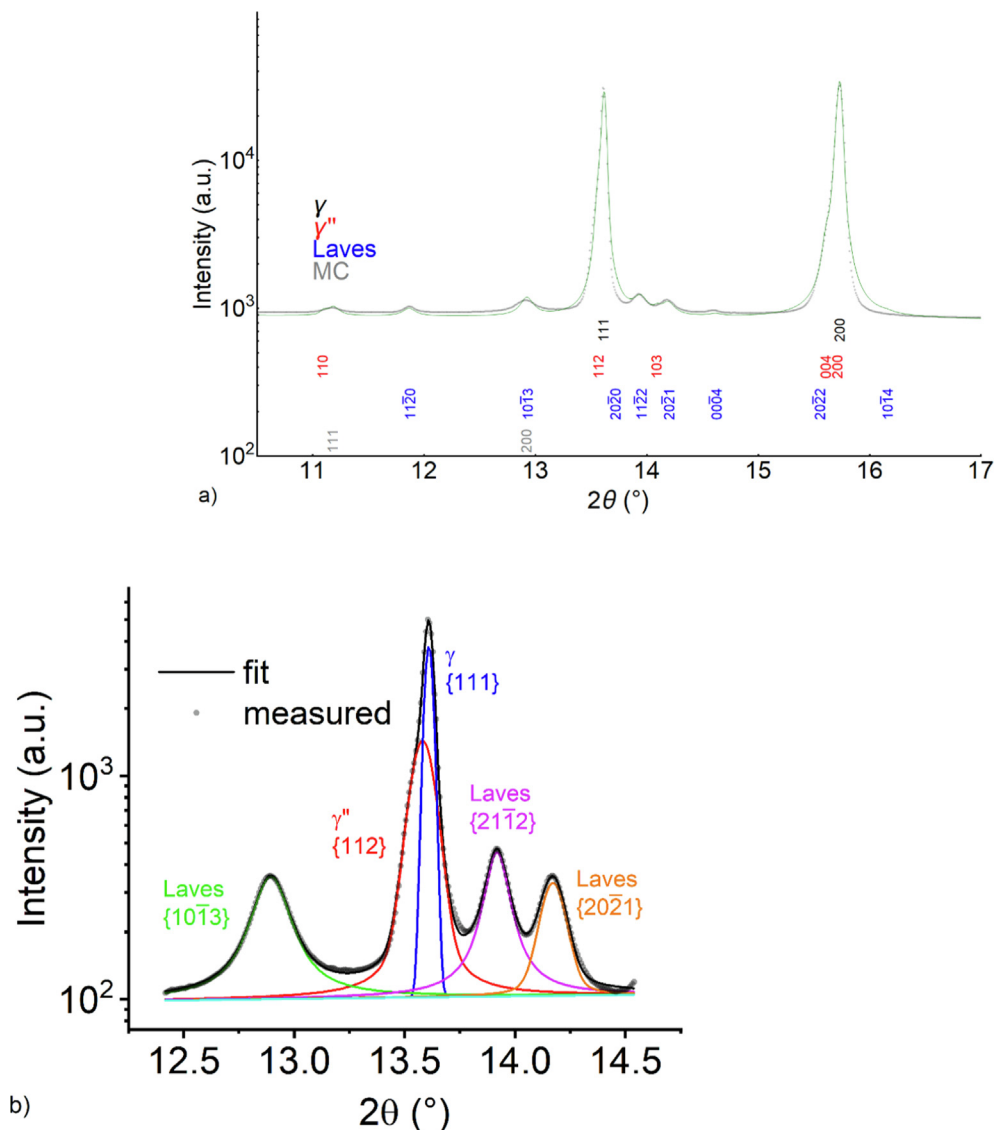

Fig. 5. (a) Rietveld refinement and (b) example of the multiple peak fitting.

Table 2
Lattice parameter and phase fraction fitted with the Rietveld analysis.

	$a(\gamma)$	$a(\gamma'')$	$c(\gamma'')$	$\gamma''/(\gamma + \gamma'')$
0 mm	3.5930	3.6015	7.2412	35.2%
0.5 mm	3.5937	3.6023	7.2445	25.1%
5 mm	3.5940	3.5801	7.2493	11.3%

and the grain morphology shown in Fig. 10a or under the scanning electron microscope using the backscattered diffraction (BSD), shown in Fig. 10b. In both images, slightly increased number of defects around the center is observed which was observed for con-

centric scanning [45]. In the BSD image, concentric circles are observed related to the phase contrast. An Energy-dispersive X-ray spectroscopy (EDX) investigation was undertaken in order to identify the source of the BSD contrast. It was observed that the precipitation contrast matches with the high concentrations of Nb (Fig. 10c and d), which in addition to the XRD analysis, it is concluded that the contrast originates from γ'' precipitates which are rich in Nb. Moreover, the γ'' precipitates preferentially form at the boundaries of the scanning lines.

Unlike the AD sample, the microstructure and the texture is strongly inhomogeneous in the CO sample, i.e. strong $\langle 110 \rangle$ -texture is observed in the building direction; however, this texture
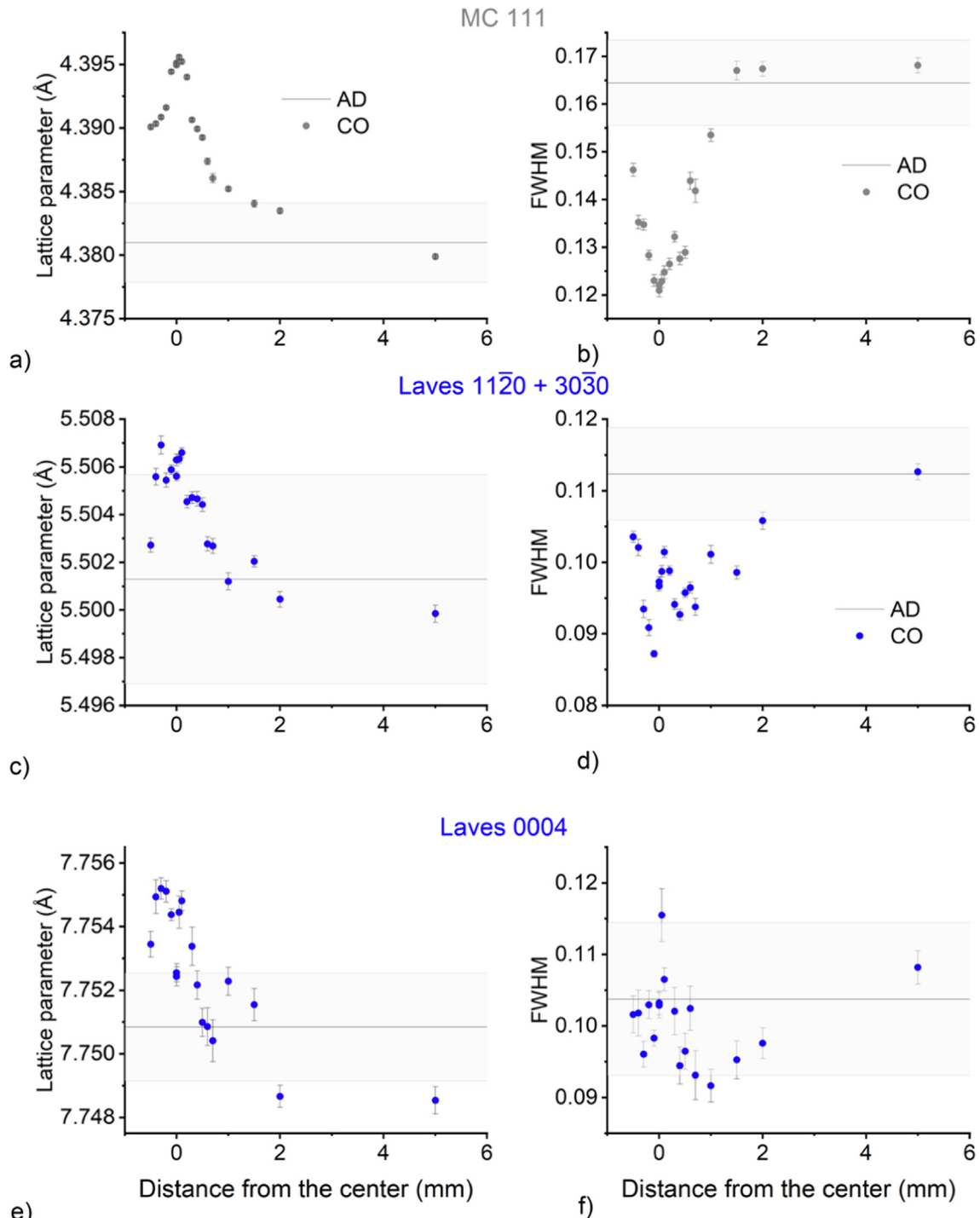

Fig. 6. (a,c,e) Lattice parameter and (b,d,f) FWHM of (a,b) Carbide and (c,d,e,f) Laves phases.
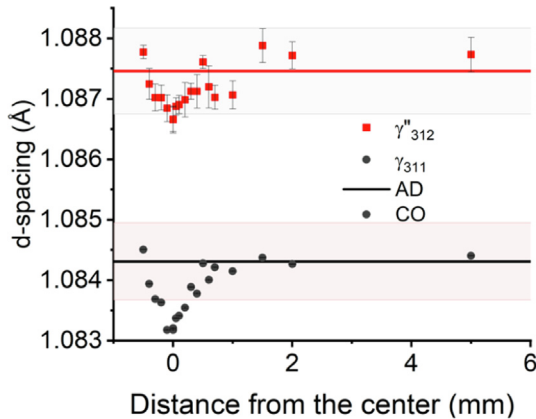
Fig. 7. Lattice spacing evolution for the {311}, peaks of the γ phase and {312} +{116} of the γ'' phase for the CO sample.

is much stronger in the center and becomes weaker towards the edge of the sample. In addition, strong $\langle 100 \rangle$-texture is observed in the hoop direction, towards the edge of the sample. These findings are in good agreement with the ND observations.

The EBSD map was also used to evaluate the grain size in the hoop direction since similar grain morphology is observed for both samples. The size of the maps used for the calculation was 1083×844 μm^2 and the distribution was calculated utilizing more than 1750 grains for each point. The grain size distribution is shown in Fig. 11a. They follow Log-normal distributions. The larger grains are at the center of the CO sample, while the smallest are at the edge, whereas the AD sample exhibits homogenous grain distribution radially (Fig. 11b).

3.4. Neutron diffraction - residual stresses

As shown in Eq. (2) the RS are calculated using the measured d-values, stress free reference d_0, Young modulus E and poisson ratio v. The residual stresses were evaluated from the lattice spacing for {311} planes shown in Fig. 4b. Acquiring a reliable d_0 has been shown to be challenging and several methods are proposed in literature [46–48]. As shown before, the pronounced variations in the type and fraction of precipitates within one sample can have significant impact on the local chemical composition. Hence, using the raw powder or annealing the samples are not appropriate due differences in chemical composition due to evaporation or precipitation respectively. Another possibility often used is cutting small cubes that are considered stress free. These cubes have to be large enough to be fully inside the beam; otherwise, pseudo strains due to the partially immersed volume could be measured. Simultaneously, they have to be small enough to release fully the stresses.

The AD sample shows a uniform microstructure throughout the whole sample volume, therefore, a single d_0 value can be used to calculate the lattice strains. After the measurement of all three components, there was still significant variation among the three components. Therefore, a different approach was followed by estimating d_0 by minimizing the sum of squares of all three stress components with respect to d_0 (Eqs. (3) and (4)). The result of the calculated d_0, compared to the "strained sample" measurements together with calculated RS are shown in Fig. 12. The obtained d_0 values for the AD sample show almost no variation through the sample. Therefore, an average value, $d_{0AD} = 1.08542 \pm 0.00005$ Å, was utilized for calculating strain.

$$\frac{d\sum_{i=1}^{3}\sigma_{ii}(d_1,d_2,d_3,d_0,E,v)^2}{dd_0} = 0 \qquad (3)$$

$$d_0 = \frac{-2(d_1d_2 + d_2d_3 + d_3d_1)(v-2)v + \left(d_1^2 + d_2^2 + d_3^2\right)(1 + v(3v-2))}{(d_1 + d_2 + d_3)(1+v)^2} \qquad (4)$$

When measured with high spatial resolution by synchrotron XRD, it is seen that the lattice spacing of the CO sample shows strong variations, as seen at Fig. 7; and therefore, using a single d_0 value for the whole sample can be disputable. The region away from the center exhibits the same d-spacing as the AD sample while the central part shows a sharp decrease in the d-spacing value (Fig. 7). Despite the observed sharp change in d-spacing it is still possible to use the single value for the whole sample. When the data from XRD are averaged over the volume that represents the ND measurement, the average value of $\bar{d_0}$, for both center and near the edge of the CO sample, are very similar within the experimental error. A full calculation is presented in the Appendix.

Another comparison of the samples can be done by calculating the von Mises stress (Eq. (5), Fig. 13). This calculation is less sensitive to the d_0 value than actual RS (eq. (6)).

$$\sigma_{VM} = \sqrt{\frac{(\sigma_{11} - \sigma_{22})^2 + (\sigma_{11} - \sigma_{33})^2 + (\sigma_{33} - \sigma_{22})^2}{2}} \qquad (5)$$

$$\sigma_{VM} = \frac{E}{d_0(1+v)}\sqrt{d_1^2 + d_2^2 + d_3^2 - d_1d_2 - d_2d_3 - d_3d_1} \qquad (6)$$

It is possible to observe that there are higher RS in the CO sample than in the AD sample. The radial and hoop stress magnitudes are approximately the same within the experimental error for the AD sample and the stress decreases towards the edge of the sample. The evolution of the stress in the CO sample is more complex. All components exhibit compressive stress in the center, higher in the radial and hoop direction. While the radial stress component relaxes towards the edge of the sample, the hoop and axial compo-
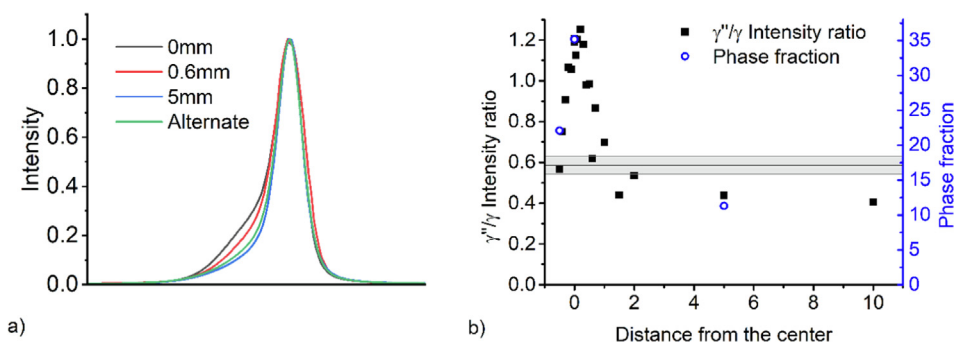

Fig. 8. (a) Comparison of the normalized 311 peaks (b) Ratio of the integrated intensity of γ''/γ and γ'' phase fraction obtained from the Rietveld refinement for the CO sample.
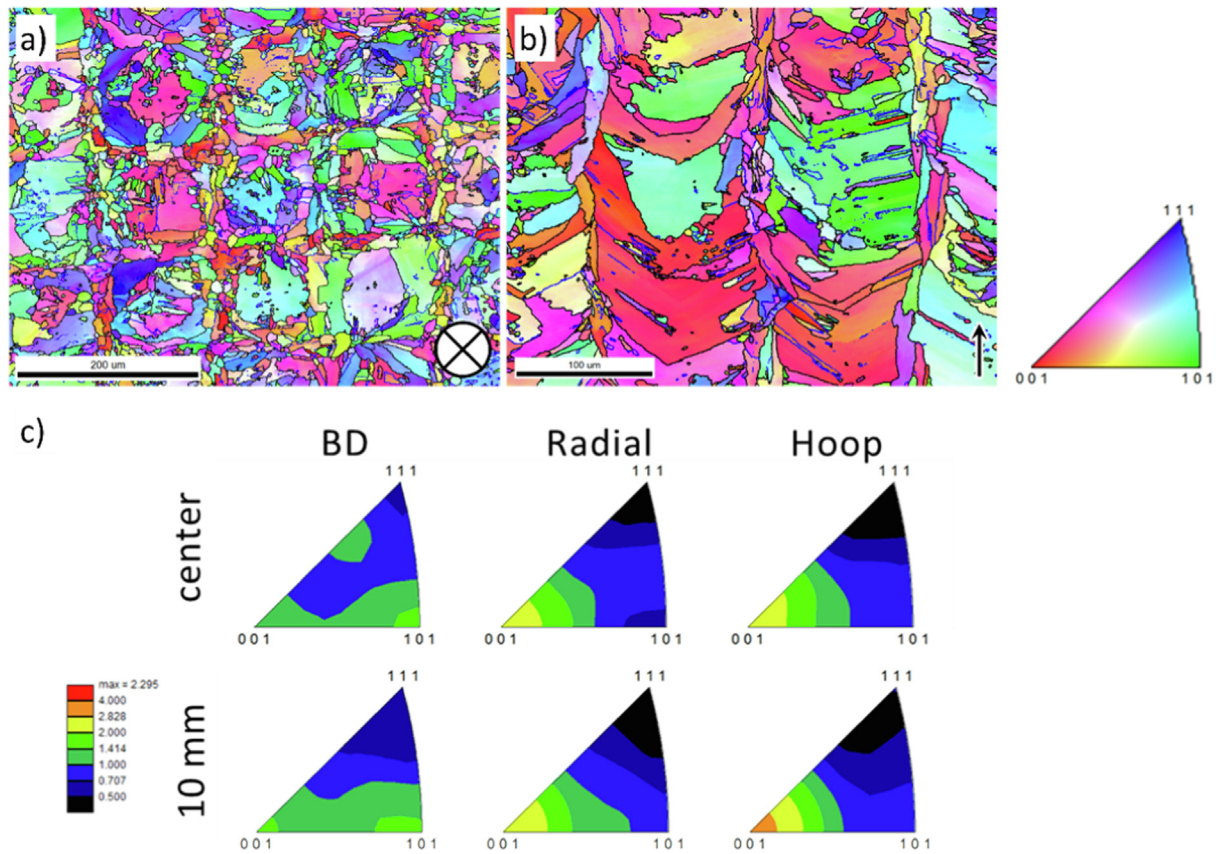
Fig. 9. EBSD map of the alternate scanning direction sample in the center of the sample. (a) in the building and (b) in the radial direction respectively. Low angle boundaries (<5°) are marked with blue line. The IPF coloring is in the out of plane direction of the map. The building direction is indicated at the bottom right of figures (a) and (b) with an X and an arrow respectively. (c) IPF calculated from EBSD maps.
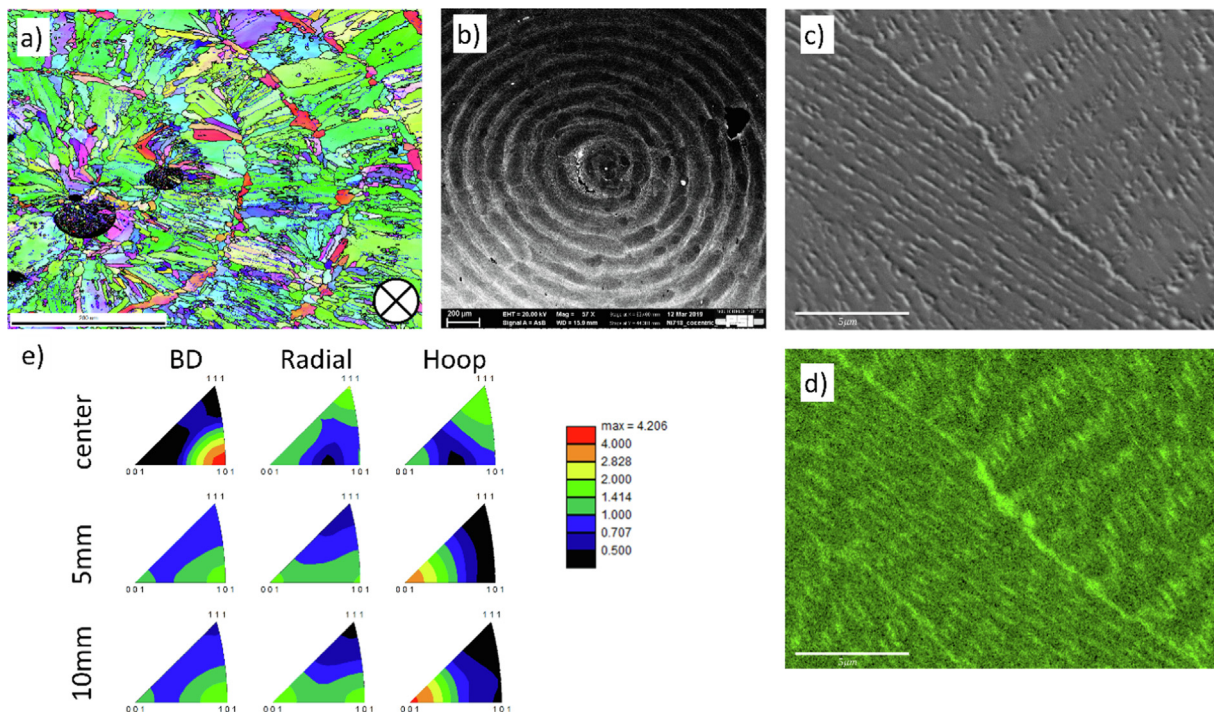

Fig. 10. Microstructure of the CO sample in the center (a) EBSD, (b) BSD SEM image showing contrast variation due to precipitation and chemical variations, (c) SE image in high magnification showing contrast due to the precipitates, (d) EDX map showing the distribution of Nb, (e) IPF calculated from EBSD maps.
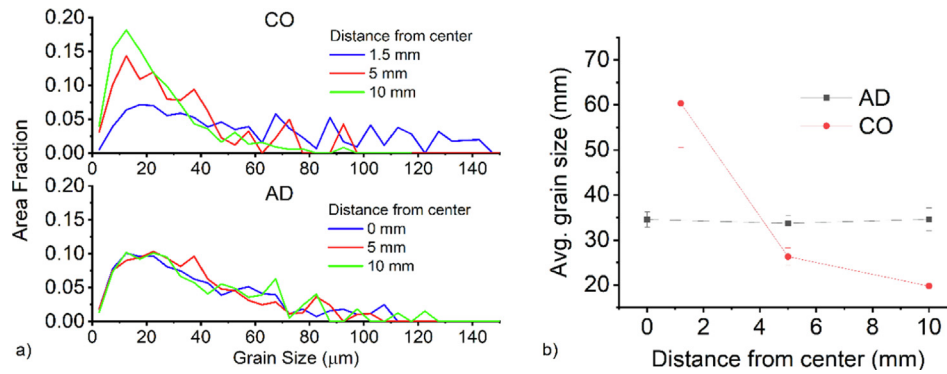
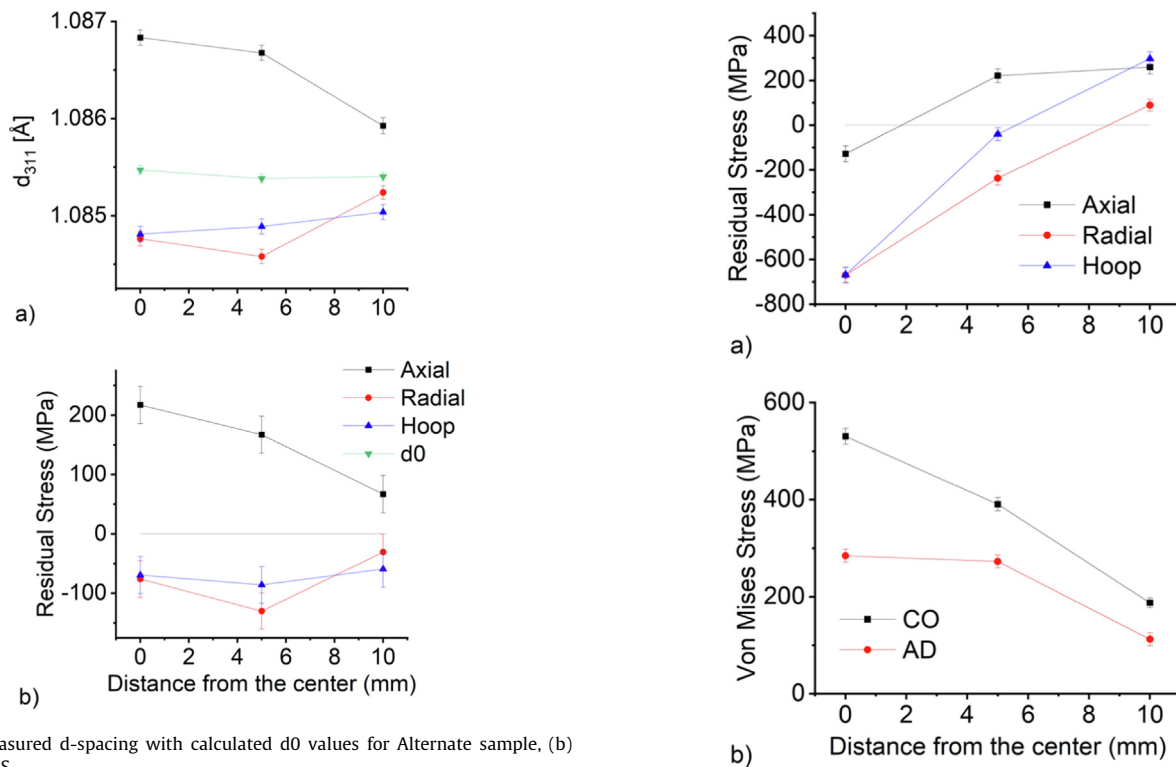**Fig. 11.** Grain size distribution for (a) AD and CO sample and (b) comparison of the average grain size.

Fig. 12. Measured d-spacing with calculated d0 values for Alternate sample, (b) calculated RS.

Fig. 13. Estimation of the RS in the (a) CO sample, (b) Von Mises stress for the AD and CO samples.

nents gradually become tensile at the edge of the sample. The Mises stress is much higher in the CO sample, in particular in the center, i.e. 528 MPa, which is less than 200 MPa below the Yield point of this material [49].

4. Discussion

The microstructure of both samples correlates well with the laser-scanning pattern. The AD scanning has the same pattern within the whole area of the sample and no significant differences are observed in terms of crystallographic texture, grain size and precipitation. As a result of the concentric scanning pattern, the laser travels shorter distance at the center before passing again at a position as compared to the edge of the sample, which results in a heat concentration at the center of the CO sample. It has been shown that the texture in the building direction is strongly influenced by the process parameters [3,6,50]. In the present material, strong $\langle 110 \rangle$ texture is observed at the center of the CO sample which is related to the heat concentration at the center of the sam-
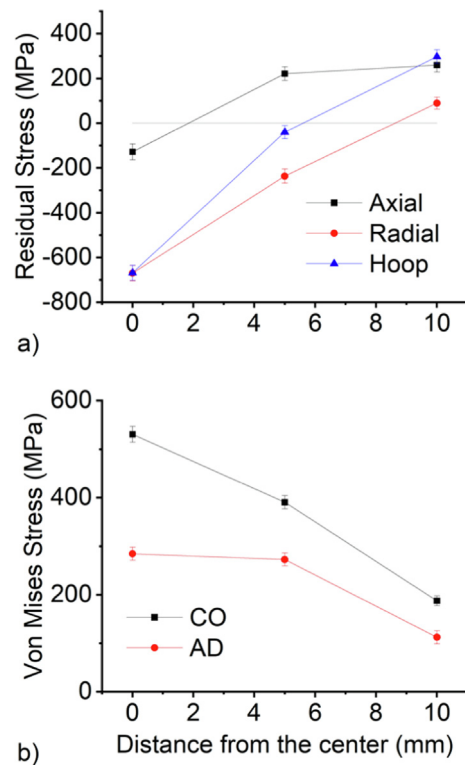
ple during the manufacturing process. For the AD sample, due to the alternate scanning strategy, the radial and hoop directions are equivalent in terms of laser scanning direction and they both exhibit a mild $\langle 100 \rangle$ texture. The 100 pole figure correlates very well with the laser path and has a stronger texture component than that for 110 in the building direction (Fig. 14). Similarly, the CO sample exhibits strong $\langle 100 \rangle$ texture along the laser scanning path. These results are consistent with previous observations of grains aligning with their [100] crystallographic direction parallel to the scanning vector and the orientation in the building direction was either [010] or [011] depending on the VED [7,51]. The texture in the building direction can be strongly influenced by the heat input, either by changing of the laser process parameters or tailoring the scanning strategies. The strongest texture component in the CO sample is the $\langle 100 \rangle$ along the laser path, where the scanning can be considered unidirectional. As such the strength of the $\langle 100 \rangle$ texture decreases towards the center of the CO sample, as shown in Fig. 10c.
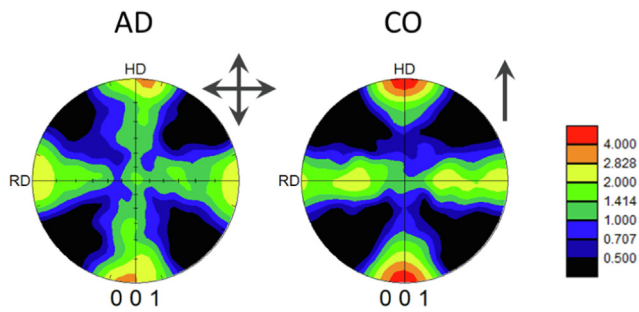
Fig. 14. 001 pole figures for the AD sample and CO sample at 10 mm from the center, RD and HD correspond to the radial and hoop directions respectively. Arrow shows the laser path direction.

The different thermal history influences also the grain morphology and defect density of the samples. The grains at the center of the CO sample are larger and columnar in shape with higher aspect ratio than the grains at the outer surface of the cylinder and the AD sample. Also higher concentration of defect was observed. All these observations have been related to samples processed with relatively high VED [3,32]. Hence, both the crystallographic texture and grain morphology are affected by the relatively high local heat input in the center of the CO sample.

The phase fraction of the γ'' phase is also strongly influenced by the different heating cycles in the middle and at the edge of the CO sample. Hence, a higher fraction of γ'' is observed at the center than the edges of the CO sample, as the material at the center experiences higher temperature for longer time, allowing increased precipitation of γ''. The high γ'' volume fraction at the center also significantly influences the γ lattice parameter, due to Nb depletion, as seen in Fig. 15 where the lattice parameter of the γ phase is inversely proportional to the fraction of γ''. The later observation is in good agreement with [52,53] where the precipitation of γ'' during isothermal annealing leads to a decrease of the lattice parameter of the γ phase. The scatter in the γ'' phase volume is probably associated with the inhomogeneous distribution of γ'' as seen at Fig. 10b. The higher volume of γ'' phase at the bottom of the sample can be explained by different thermal cycles in the proximity of the pre-heated base plate [54]. The carbides exhibit also a difference in lattice parameter, which is also an indication of chemical variations in the CO sample.

The local chemical variation in the CO sample complicates significantly the calculation of the residual stress and the choice of reliable d_0 values. However, a reliable method for estimating a reference d_0 value is proposed based on several measurements utilizing XRD and ND methods. Tensile stresses are thus calculated in the building direction and compressive stresses in radial and hoop direction of AD sample. It is apparent that the homogenous scan-

ning pattern of the AD sample results in relatively homogenous RS in the sample in the range of 150 to 200 MPa in the building direction and −100 to −150 MPa in the radial and hoop directions. The strong compressive stresses in the center of the CO sample are a result of the high concentration of heat input. Therefore, the magnitude of the RS significantly decreases towards the edge of the sample.

5. Conclusions

Cylindrical samples from Alloy 718 were LPBF manufactured using the same processing parameters but two different scanning patterns, namely alternate line scans and concentric circular scans from the outer towards the center of the cylinder. A detailed synchrotron X-ray diffraction investigation revealed differences in the volume fraction of the γ'' precipitates and variation of the lattice parameter of the Laves and carbide phases due to different chemical compositions in the concentric scanned sample. Electron microscopy also shows that the γ'' phase precipitates are located at the boundaries of the laser tracks in the concentric scanned sample. The crystallographic texture of the concentric scanned sample is heterogeneous, i.e. strong $\langle 110 \rangle$ texture along the building direction is observed at the center which becomes less strong towards the edge of the sample. Relatively strong $\langle 110 \rangle$ -texture is observed in the radial direction for both samples. The concentric scanned sample exhibits larger columnar grains than the edges or the alternate scanned sample. The observed differences are due to the heat concentration at the center of the concentric scanned sample, whereas the alternate direction of the laser in the alternate scanned sample results in a more homogeneous distribution of heat and hence more homogenous microstructure in terms of precipitation, grain size and morphology. The different extent of precipitation affects the chemical composition of the matrix γ and results in a variation of the reference d_0 value. In particular, the lattice parameter of the matrix is inversely proportional to the volume fraction of γ'' phase precipitates. A reliable stress free sample for the ND measurement is difficult to obtain. Therefore, measurements with high spatial resolution were obtained with XRD and averaged so that they match the gauge volume of the ND measurements. A reliable reference d_0 value is obtained by minimizing the sum of squares of all three components with respect to d_0. The obtained residual stress results are reasonable considering the symmetries of both scanning strategies.

Data availability

The raw/processed data required to reproduce these findings cannot be shared at this time as the data also forms part of an ongoing study.

Declaration of Competing Interest

The authors declare that they have no known competing financial interests or personal relationships that could have appeared to influence the work reported in this paper.

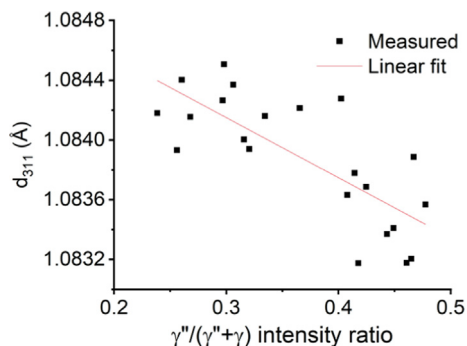## Acknowledgement

Fig. 15. Dependence of the $d_{0.311}$ on the γ'' volume fraction.

Appendix

Rationale for using of the single d_0 in the concentric sample

When measuring a line scan with small step size, using synchrotron XRD, the difference between the d-spacing value in the center and at the edge is 1.4×10^{-3} Å, which can be misinterpreted as a pseudostrains of 1300 $\mu\varepsilon$ in magnitude. The shift of the averaged d_0 value in the center can be estimated by fitting the lattice spacing measured with XRD (Fig. 7), weighted over the beam profile. The data were fitted with a pseudo-Voight function (Eq. (7)) which is the linear combination of Gaussian and Lorentzian curve.

$$f_{d_{311}}(d_0, A, \sigma, \mu, r_0, r) = d_0 - \pi A$$
$$\times \sqrt{\sigma} \left(\sqrt{\frac{\ln 2}{\pi\sigma}} \mu 2^{-\frac{4(r-r_0)^2}{\sigma^2}} + \frac{(1-\mu)\sigma}{\pi(\sigma^2 + 4(r-r_0)^2)} \right)$$

(7)

d_0 is the lattice spacing away from the center, A is the amplitude, σ defines the width of the peak, μ is the scaling between the Lorentzian and Gaussian contribution, r_0 is the center of the distribution and r is the position. The parameters obtained by the fit are shown in Table 3.

The neutron gauge volume is given by the beam profile of POLDI and its detector radial collimator and it can be approximated by a 2D Gaussian function (Eq. (8)), where σ_{col} is given by the collimator and σ_{beam} by the beam profile. For the current measurement a radial collimator with FWHM of 3.8 mm was used, which gives $\sigma_{col} = 3.8/2\sqrt{2\ln 2}$ mm. The combination of the beam profile and horizontal slit opening of 3.8 mm allow us to use the same value for σ_{beam}.

$$\omega_{GV}(\sigma_{col}, \sigma_{beam}, x, y) = E^{-\frac{x^2}{2\sigma_{col}^2} - \frac{y^2}{2\sigma_{beam}^2}}$$

(8)

For calculating the average d-spacing value within the neutron gauge volume, the equation for continuous weighted average is used (Eq. (9)), where $\bar{f}$ is the average value of the function $f(x)$ and $\omega(x)$ is the weight function.

$$\bar{f} = \frac{\int f(x)\omega(x)dx}{\int \omega(x)}$$

(9)

$$\bar{d_0} = \frac{\int f_{d_{311}}(d_0, A, \sigma, \mu, x_0, x, y_0, y)\omega_{GV}(\sigma_{col}, \sigma_{beam}, x, y)dxdy}{\int \omega_{GV}(\sigma_{col}, \sigma_{beam}, x, y)dxdy}$$

(10)

where $(r - r_0)^2 = (x - x_0)^2 + (y - y_0)^2$ is the transformation between the cylindrical and Cartesian coordinates in Eqs. (7) and (10).

By evaluating Eq. (10) an estimation of the mean value of $\bar{d_0}$ in the center as 1.08428 Å, is obtained. The difference between d_0 (away from the center) and $\bar{d_0}$ (at the center) is 2×10^{-5} Å which is less than the experimental error and it introduces a strain uncertainty of only 18 $\mu\varepsilon$. Therefore, it is possible to use a single d_0 value for the neutron diffraction experiment on the stress distribution of the CO sample.

Table 3
Fitted parameters for the 311 lattice spacing.

d_0 [Å]	A [Å]	σ	μ	x_0 [mm]
1.0843 ± 0.0001	0.0011 ± 0.0001	0.56 ± 0.08	0.5 ± 0.7	-0.01 ± 0.02

References

[1] Q. Jia, D. Gu, Selective laser melting additive manufacturing of Inconel 718 superalloy parts: densification, microstructure and properties, J. Alloys Compd. 585 (2014) 713–721.

[2] V.A. Popovich, E.V. Borisov, A.A. Popovich, V.S. Sufiiarov, D.V. Masaylo, L. Alzina, Functionally graded Inconel 718 processed by additive manufacturing: crystallographic texture, anisotropy of microstructure and mechanical properties, Mater. Des. 114 (2017) 441–449.

[3] Z. Sun, X. Tan, S.B. Tor, C.K. Chua, Simultaneously enhanced strength and ductility for 3D-printed stainless steel 316L by selective laser melting, NPG Asia Mater. 10 (4) (2018) 127–136.

[4] C. Sofras, J. Čapek, A. Arabi-Hashemi, C. Leinenbach, M. Frost, K. An, R.E. Logé, M. Strobl, E. Polatidis, Tailored deformation behavior of 304L stainless steel through control of the crystallographic texture with laser-powder bed fusion, Mater. Des. 219 (2022) 110789.

[5] N. Read, W. Wang, K. Essa, M.M. Attallah, Selective laser melting of AlSi10Mg alloy: process optimisation and mechanical properties development, Mater. Des. (1980–2015) 65 (2015) 417–424.

[6] M. Higashi, T. Ozaki, Selective laser melting of pure molybdenum: Evolution of defect and crystallographic texture with process parameters, Mater. Des. 191 (2020) 108588.

[7] S.-H. Sun, T. Ishimoto, K. Hagihara, Y. Tsutsumi, T. Hanawa, T. Nakano, Excellent mechanical and corrosion properties of austenitic stainless steel with a unique crystallographic lamellar microstructure via selective laser melting, Scripta Mater. 159 (2019) 89–93.

[8] X. Liu, C. Zhao, X. Zhou, Z. Shen, W. Liu, Microstructure of selective laser melted AlSi10Mg alloy, Mater. Des. 168 (2019) 107677.

[9] D.D. Gu, W. Meiners, K. Wissenbach, R. Poprawe, Laser additive manufacturing of metallic components: materials, processes and mechanisms, Int. Mater. Rev. 57 (3) (2012) 133–164.

[10] M. Masoomi, N. Shamsaei, R.A. Winholtz, J.L. Milner, T. Gnäupel-Herold, A. Elwany, M. Mahmoudi, S.M. Thompson, Residual stress measurements via neutron diffraction of additive manufactured stainless steel 17–4 PH, Data Brief 13 (2017) 408–414.

[11] T. Thiede, S. Cabeza, T. Mishurova, N. Nadammal, A. Kromm, J. Bode, C. Haberland, G. Bruno, Residual stress in selective laser melted inconel 718: influence of the removal from base plate and deposition hatch length, Mater. Perform. Character. 7 (4) (2018) 717–735.

[12] M. Larsson, P. Hedenqvist, S. Hogmark, Deflection measurements as method to determine residual stress in thin hard coatings on tool materials, Surf. Eng. 12 (1) (1996) 43–48.

[13] A. Salmi, E. Atzeni, L. Iuliano, M. Galati, Experimental analysis of residual stresses on AlSi10Mg parts produced by means of Selective Laser Melting (SLM), Proc. CIRP 62 (2017) 458–463.

[14] H. Ali, H. Ghadbeigi, K. Mumtaz, Effect of scanning strategies on residual stress and mechanical properties of Selective Laser Melted Ti6Al4V, Mater. Sci. Eng.: A 712 (2018) 175–187.

[15] Y. Lu, S. Wu, Y. Gan, T. Huang, C. Yang, L. Junjie, J. Lin, Study on the microstructure, mechanical property and residual stress of SLM Inconel-718 alloy manufactured by differing island scanning strategy, Opt. Laser Technol. 75 (2015) 197–206.

[16] M.F. Zaeh, G. Branner, Investigations on residual stresses and deformations in selective laser melting, Prod. Eng. 4 (1) (2010) 35–45.

[17] Y. Wang, J. Shi, Y. Liu, Competitive grain growth and dendrite morphology evolution in selective laser melting of Inconel 718 superalloy, J. Cryst. Growth 521 (2019) 15–29.

[18] G.H. Cao, T.Y. Sun, C.H. Wang, X. Li, M. Liu, Z.X. Zhang, P.F. Hu, A.M. Russell, R. Schneider, D. Gerthsen, Z.J. Zhou, C.P. Li, G.F. Chen, Investigations of γ', γ'' and δ precipitates in heat-treated Inconel 718 alloy fabricated by selective laser melting, Mater. Character. 136 (2018) 398–406.

[19] E. Chlebus, K. Gruber, B. Kuźnicka, J. Kurzac, T. Kurzynowski, Effect of heat treatment on the microstructure and mechanical properties of Inconel 718 processed by selective laser melting, Mater. Sci. Eng.: A 639 (2015) 647–655.

[20] P. Karimi, T. Raza, J. Andersson, L.-E. Svensson, Influence of laser exposure time and point distance on 75-µm-thick layer of selective laser melted Alloy 718, Int. J. Adv. Manuf. Technol. 94 (5–8) (2018) 2199–2207.

[21] T. Raza, J. Andersson, L.-E. Svensson, Microstructure of selective laser melted alloy 718 in as-manufactured and post heat treated condition, Proc. Manuf. 25 (2018) 450–458.

[22] W. Tillmann, C. Schaak, J. Nellesen, M. Schaper, M.E. Aydinöz, K.-P. Hoyer, Hot isostatic pressing of IN718 components manufactured by selective laser melting, Add. Manuf. 13 (2017) 93–102.

[23] A. Kreitcberg, V. Brailovski, S. Turenne, Effect of heat treatment and hot isostatic pressing on the microstructure and mechanical properties of Inconel 625 alloy processed by laser powder bed fusion, Mater. Sci. Eng.: A 689 (2017) 1–10.

[24] Z. Wang, K. Guan, M. Gao, X. Li, X. Chen, X. Zeng, The microstructure and mechanical properties of deposited-IN718 by selective laser melting, J. Alloys Compd. 513 (2012) 518–523.

[25] B.o. Cheng, S. Shrestha, K. Chou, Stress and deformation evaluations of scanning strategy effect in selective laser melting, Add. Manuf. 12 (2016) 240–251.

[26] A.V. Gusarov, M. Pavlov, I. Smurov, Residual stresses at laser surface remelting and additive manufacturing, Phys. Proc. 12 (2011) 248–254.

[27] R.K.R. Vignesh, M. Kiriti, R. Bharath, F. Behzad, A. Amirhesam, M. Narges Shayesteh, Determination of residual stress for Inconel 718 samples fabricated through different scanning strategies in selective laser melting, in: Proc. SPIE, 2020.

[28] S. Holland, X. Wang, J. Chen, W. Cai, F. Yan, L. Li, Multiscale characterization of microstructures and mechanical properties of Inconel 718 fabricated by selective laser melting, J. Alloys Compd. 784 (2019) 182–194.

[29] A. Hussein, L. Hao, C. Yan, R. Everson, Finite element simulation of the temperature and stress fields in single layers built without-support in selective laser melting, Mater. Des. 52 (2013) 638–647.

[30] C. Tang, J.L. Tan, C.H. Wong, A numerical investigation on the physical mechanisms of single track defects in selective laser melting, Int. J. Heat Mass Transfer 126 (2018) 957–968.

[31] X. Wang, K. Chou, Microstructure simulations of Inconel 718 during selective laser melting using a phase field model, Int. J. Adv. Manuf. Technol. 100 (9–12) (2019) 2147–2162.

[32] L. Parry, I.A. Ashcroft, R.D. Wildman, Understanding the effect of laser scan strategy on residual stress in selective laser melting through thermo-mechanical simulation, Add. Manuf. 12 (2016) 1–15.

[33] H. Yang, L. Meng, S. Luo, Z. Wang, Microstructural evolution and mechanical performances of selective laser melting Inconel 718 from low to high laser power, J. Alloys Compd. 828 (2020) 154473.

[34] O. Arnold, J.C. Bilheux, J.M. Borreguero, A. Buts, S.I. Campbell, L. Chapon, M. Doucet, N. Draper, R. Ferraz Leal, M.A. Gigg, V.E. Lynch, A. Markvardsen, D.J. Mikkelson, R.L. Mikkelson, R. Miller, K. Palmen, P. Parker, G. Passos, T.G. Perring, P.F. Peterson, S. Ren, M.A. Reuter, A.T. Savici, J.W. Taylor, R.J. Taylor, R. Tolchenov, W. Zhou, J. Zikovsky, Mantid—data analysis and visualization package for neutron scattering and μ SR experiments, Nucl. Instrum. Meth. Phys. Res. Sect. A: Accel. Spectrom. Detect. Assoc. Equip. 764 (2014) 156–166.

[35] Z. Wang, E. Denlinger, P. Michaleris, A.D. Stoica, D. Ma, A.M. Beese, Residual stress mapping in Inconel 625 fabricated through additive manufacturing: method for neutron diffraction measurements to validate thermomechanical model predictions, Mater. Des. 113 (2017) 169–177.

[36] P.E. Aba-Perea, T. Pirling, P.J. Withers, J. Kelleher, S. Kabra, M. Preuss, Determination of the high temperature elastic properties and diffraction elastic constants of Ni-base superalloys, Mater. Des. 89 (2016) 856–863.

[37] J.M. Oblak, D.S. Duvall, D.F. Paulonis, An estimate of the strengthening arising from coherent, tetragonally-distorted particles, Mater. Sci. Eng. 13 (1) (1974) 51–56.

[38] D. Deng, R.L. Peng, H. Brodin, J. Moverare, Microstructure and mechanical properties of Inconel 718 produced by selective laser melting: sample orientation dependence and effects of post heat treatments, Mater. Sci. Eng.: A 713 (2018) 294–306.

[39] C. Slama, M. Abdellaoui, Structural characterization of the aged Inconel 718, J. Alloys Compd. 306 (1–2) (2000) 277–284.

[40] S. Azadian, L.-Y. Wei, R. Warren, Delta phase precipitation in Inconel 718, Mater. Charact. 53 (1) (2004) 7–16.

[41] M. Sundararaman, P. Mukhopadhyay, S. Banerjee, Precipitation of the δ-Ni3Nb phase in two nickel base superalloys, Metall. Trans. A 19 (3) (1988) 453–465.

[42] V. Dyadkin, P. Pattison, V. Dmitriev, D. Chernyshov, A new multipurpose diffractometer PILATUS@SNBL, J. Synchrotron Radiat. 23 (3) (2016) 825–829.

[43] B.H. Toby, R.B. Von Dreele, GSAS-II: the genesis of a modern open-source all purpose crystallography software package, J. Appl. Crystallogr. 46 (2) (2013) 544–549.

[44] O. Andreau, I. Koutiri, P. Peyre, J.-D. Penot, N. Saintier, E. Pessard, T. De Terris, C. Dupuy, T. Baudin, Texture control of 316L parts by modulation of the melt pool morphology in selective laser melting, J. Mater. Process. Technol. 264 (2019) 21–31.

[45] L. Englert, V. Schulze, S. Dietrich, Concentric scanning strategies for laser powder bed fusion: porosity distribution in practical geometries, Materials 15 (3) (2022) 1105.

[46] S. Goel, M. Neikter, J. Capek, E. Polatidis, M.H. Colliander, S. Joshi, R. Pederson, Residual stress determination by neutron diffraction in powder bed fusion-built Alloy 718: Influence of process parameters and post-treatment, Mater. Des. 195 (2020) 109045.

[47] K.e. An, L. Yuan, L. Dial, I. Spinelli, A.D. Stoica, Y. Gao, Neutron residual stress measurement and numerical modeling in a curved thin-walled structure by laser powder bed fusion additive manufacturing, Mater. Des. 135 (2017) 122–132.

[48] P.J. Withers, M. Preuss, A. Steuwer, J.W.L. Pang, Methods for obtaining the strain-free lattice parameter when using diffraction to determine residual stress, J. Appl. Crystallogr. 40 (5) (2007) 891–904.

[49] J. Čapek, E. Polatidis, M. Knapek, C. Lyphout, N. Casati, R. Pederson, M. Strobl, The Effect of γ″ and δ phase precipitation on the mechanical properties of inconel 718 manufactured by selective laser melting: an in situ neutron diffraction and acoustic emission study, JOM 73 (1) (2021) 223–232.

[50] J.J. Marattukalam, D. Karlsson, V. Pacheco, P. Beran, U. Wiklund, U. Jansson, B. Hjörvarsson, M. Sahlberg, The effect of laser scanning strategies on texture, mechanical properties, and site-specific grain orientation in selective laser melted 316L SS, Mater. Des. 193 (2020) 108852.

[51] K.A. Sofinowski, S. Raman, X. Wang, B. Gaskey, M. Seita, Layer-wise engineering of grain orientation (LEGO) in laser powder bed fusion of stainless steel 316L, Add. Manuf. 38 (2021) 101809.

[52] R.Y. Zhang, H.L. Qin, Z.N. Bi, J. Li, S. Paul, T.L. Lee, S.Y. Zhang, J. Zhang, H.B. Dong, Evolution of lattice spacing of gamma double prime precipitates during aging of polycrystalline Ni-base superalloys: an in situ investigation, Metall. Mater. Trans. A 51 (2) (2020) 574–585.

[53] H. Qin, Z. Bi, D. Li, R. Zhang, T.L. Lee, G. Feng, H. Dong, J. Du, J. Zhang, Study of precipitation-assisted stress relaxation and creep behavior during the ageing of a nickel-iron superalloy, Mater. Sci. Eng.: A 742 (2019) 493–500.

[54] A. Seidel, S. Saha, T. Maiwald, J. Moritz, S. Polenz, A. Marquardt, J. Kaspar, T. Finaske, E. Lopez, F. Brueckner, C. Leyens, Intrinsic heat treatment within additive manufacturing of gamma titanium aluminide space hardware, JOM 71 (4) (2019) 1513–1519.